

CAN CHANDRA RESOLVE THE REMAINING COSMIC X-RAY BACKGROUND?

RYAN C. HICKOX AND MAXIM MARKEVITCH¹

Harvard-Smithsonian Center for Astrophysics, 60 Garden Street, Cambridge, MA 02138

Accepted for publication in *The Astrophysical Journal*

ABSTRACT

The deepest extragalactic X-ray observation, the 2 Ms Chandra Deep Field North (CDF-N), resolves $\sim 80\%$ of the total extragalactic cosmic X-ray background (CXB) in the 1–2 keV band. Recent work has shown that 70% of the remaining CXB flux is associated with sources detected by the *Hubble Space Telescope* (*HST*). This paper uses the existing CDF-N data to constrain the X-ray flux distribution of these X-ray-undetected *HST* sources by comparing the number of 0.5–2 keV X-ray counts at the *HST* positions to those expected for model flux distributions. In the simple case where all the undetected *HST* X-ray sources have the same 0.5–2 keV flux, the data are best fit by 1.5–3 counts per source in 2 Ms, compared to a detection limit (at 10% completeness) of 9 counts. Assuming a more realistic power-law $\log N - \log S$ distribution [$N(> S) \propto S^{-\alpha}$], the data favor a relatively steep flux distribution, with $\alpha = 1.1^{+0.5}_{-0.3}$ (limits are 99% confidence). This slope is very similar to that previously found for faint normal and starburst galaxies in the CDF-N. These results suggest deeper *Chandra* observations will detect a new population of faint X-ray sources, but extremely deep exposures are needed to resolve the remainder of the soft CXB. In the most optimistic scenario, when the *HST* sources have the flattest allowed flux distribution and all the sources without *HST* counterparts are detected, observations 5 times more sensitive than the existing ones would resolve at most $\sim 60\%$ of the remaining soft CXB.

Subject headings: methods: data analysis — X-rays: diffuse background — X-rays: galaxies

1. INTRODUCTION

Deep X-ray observations, in particular the 1 and 2 Ms Chandra Deep Fields North and South (CDF-N and CDF-S), have resolved most of the extragalactic cosmic X-ray background (CXB) at energies $E < 4$ keV into discrete X-ray sources (see Brandt & Hasinger 2005, for a review). The spectrum of the still-unresolved CXB in the CDFs was directly measured by Hickox & Markevitch (2006, hereafter HM06), who found that $23\% \pm 3\%$ of the CXB in the 1–2 keV band remained unresolved. There is also an unresolved component at energies $E > 2$ keV, but the uncertainties are larger. In the 1–2 keV band, most of the unresolved flux can be accounted for by galaxies that are detected in deep *Hubble Space Telescope* (*HST*) observations, but are too faint to be detected as individual X-ray sources. A stacking analysis by Worsley et al. (2006) showed a significant contribution from X-ray-undetected *HST* sources. Hickox & Markevitch (2007, hereafter HM07) measured the remaining CXB spectrum after excluding all sources detected by *HST* or by the Infrared Array Camera (IRAC) on the *Spitzer Space Telescope*, and found that only $7\% \pm 3\%$ of the total 1–2 keV CXB remained.

There has been significant interest in using deeper *Chandra* observations to resolve even more of the CXB, especially since longer *Chandra* exposures might probe a new population of sources. A simple extrapolation of the total observed $\log N - \log S$ distribution [which, fitted by a power law of the form $N(> S) \propto S^{-\alpha}$, has $\alpha \simeq 0.7$] falls far short of accounting for the entire 1–2 keV CXB. If the remaining signal is due to discrete sources, an upturn in the $\log N - \log S$ at low fluxes is required (HM06). Evidence for a possible upturn in the $\log N - \log S$ distribution at $S_{0.5-2 \text{ keV}} \lesssim 10^{-17}$ ergs s^{−1} was found through a fluctuation analysis using the first 1 Ms of CDF-N data (Miyaji & Griffiths 2002).

These faint objects, with fluxes less than the faintest CDF-N

sources ($S_{0.5-2 \text{ keV}} = 2.4 \times 10^{-17}$ ergs cm^{−2} s^{−1}) are likely starburst and normal galaxies, unlike the majority of the detected X-ray sources in the CDFs, of which $\gtrsim 75\%$ are active galactic nuclei (AGNs). Bauer et al. (2004, hereafter B04) divided the CDF X-ray sources into galaxy and AGN subsets, based on their X-ray and optical properties, and produced separate $\log N - \log S$ fits to each using power law models. AGNs have a shallow $\log N - \log S$ slope with $\alpha \simeq 0.6$, while the galaxies have a much steeper distribution with $\alpha \simeq 1.3$. The galaxies may dominate the source counts at fluxes $\lesssim 10^{-17}$ ergs s^{−1}, and could produce the upturn in the $\log N - \log S$ distribution at low fluxes.

The goal of this paper is to constrain the distribution of X-ray fluxes for the *HST* sources that are cumulatively responsible for most of the unresolved 1–2 keV CXB. This study puts limits on the $\log N - \log S$ distribution only for objects with *HST* counterparts, not all unresolved X-ray sources (which would require a fluctuation analysis without the advantage of positional information). However, since X-ray-undetected *HST* sources account for $\sim 70\%$ of the unresolved 1–2 keV CXB (or $\sim 16\%$ of the total CXB), this analysis provides useful limits on the properties of X-ray sources fainter than the current CDF-N limit and puts constraints on what might be observed with longer *Chandra* exposures.

2. OBSERVATIONS

The CDF-N consists of 20 separate *Chandra* ACIS-I observations with a total exposure time of $\simeq 2$ Ms (Brandt et al. 2001; Alexander et al. 2003, hereafter A03). For this analysis, we utilize the coadded image of the CDF-N in the 0.5–2 keV band that was used for source detection by A03 (see their Fig. 3). The ACIS pixel scale is $0.492''$, and the effective aimpoint (the exposure weighted centroid of the 20 slightly offset observations) is (α , δ , J2000) 12:36:45.9, +62:13:58. We also use the 0.5–2 keV exposure map shown in Fig. 5 of A03.² The image has a total on-axis exposure time of 1.94 Ms, although the effective exposures at certain positions within our region

¹ Also at Space Research Institute, Russian Academy of Sciences, Profsoyuznaya 84/32, Moscow 117997, Russia

of interest are as low as 1.2 Ms because of the chip gaps. The on-axis exposure is ~ 2 times longer than that used in HM07, in which we filtered the data extensively for background flares (see § 3.1).

The nominal flux limit of the A03 catalog is $\approx 2.4 \times 10^{-17}$ ergs s $^{-1}$, or ≈ 9 counts in 1.94 Ms. This corresponds roughly to the flux of the faintest detected sources, for which the source detection is highly incomplete. The completeness of the CDF-N source detection depends on measured source counts, as shown in Fig. 2 (a) of B04. Within $2'$ from the aimpoint, the completeness is near zero for < 8 observed counts, and rises from $\approx 10\%$ for 10 counts to $\approx 90\%$ for 20 counts. We use this completeness curve in our modeling of the undetected X-ray sources.

The *HST* catalog of sources is the same as we used in HM07 and comes from the Great Observatories Origins Deep Survey (GOODS; Dickinson et al. 2003). Data were taken using the Advanced Camera for Surveys (ACS) on *HST* in the B_{435} , V_{606} , i_{775} , and z_{850} bands (Giavalisco et al. 2004). We use the public catalog³ for the z_{850} band (sampling wavelengths ~ 8300 – 9500 Å), which has an approximate magnitude limit of $z_{850} \simeq 27$ (AB) and nominal positional uncertainty of $\approx 0.1''$. HM07 also excluded *Spitzer* IRAC sources, but 90% of these also had *HST* counterparts, so we do not consider them here.

We slightly shift the positions of the *HST* sources to best match the positions of the brightest 100 A03 X-ray sources. This small offset of $-0.11''$ in α and $-0.28''$ in δ serves to register the coordinate frames to $\approx 0.1''$ within $2'$ of the X-ray aim point. The positional uncertainties of the *HST* sources are significantly smaller than the ACIS pixel scale and so will not affect our results.

3. ANALYSIS

Worsley et al. (2006) and HM07 showed that *HST* sources that do not have X-ray detections in the A03 catalog nonetheless contribute significant flux to the CXB. Although we cannot measure X-ray fluxes for these sources individually, the *distribution* of observed counts at the source positions can provide a useful constraint on their underlying X-ray flux distribution.

3.1. Measurement of the observed counts distribution

To measure this counts distribution, we extract 0.5–2 keV photons at the *HST* source positions in circular regions of radius r_{90} , which is an approximation of the 90% point-spread function (PSF) energy enclosed radius and varies as⁴:

$$r_{90} = 1'' + 10''(\theta/10')^2, \quad (1)$$

where θ is the off-axis angle. Because r_{90} increases with θ , at large angles many of the *HST* source regions begin to overlap. Within a $1'$ radius of the aimpoint, the regions overlap over only 9% of their area, while within a $4'$ radius, 28% of the area overlaps. To include sufficient numbers of sources but still have minimal overlap, we confine our analysis to a small region of radius $2.2'$ around the aimpoint, for which r_{90} is between 2 and 3 ACIS pixels ($1'' < r_{90} < 1.5''$) and overlap is only 12%. Using a model of the *Chandra* PSF as described in § 3.2, we find that for sources within the $2.2'$ radius,

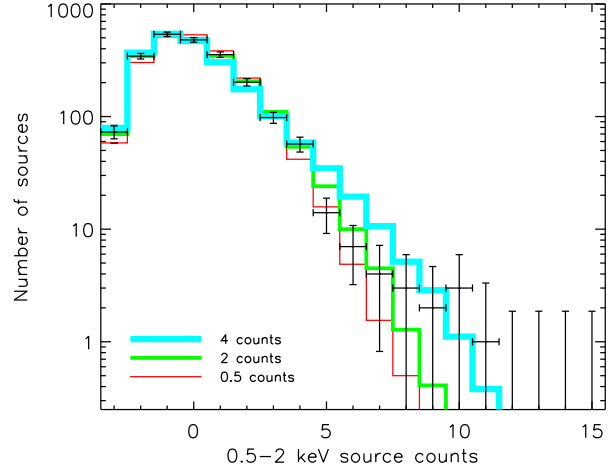


FIG. 1.— Histogram of background-subtracted 0.5–2 keV source counts inside the 2184 *HST* source regions (black crosses). Solid lines show predictions for models with “delta-function” flux distribution, consisting only of sources with fluxes of 0.5, 2, and 4 counts, respectively, per 2 Ms.

the flux scattered outside the r_{90} circles is 9.9%, accounting for the source overlap. In order to exclude the flux from detected X-ray sources, we only consider those *HST* sources that are outside large exclusion regions of $4.5r_{90}$ – $9r_{90}$ around the A03 sources, which exclude $> 99.9\%$ of the flux from these sources (see § 3.2 of HM06). We also exclude one extended source from the catalog of Bauer et al. (2002), with an exclusion region of radius $0.75'$, or 1.5 times the measured source extent. This leaves $N_{HST} = 2184$ *HST* sources over an area of 12.2 arcmin 2 .

We focus our analysis on the 0.5–2 keV band, as opposed to the 1–2 keV band as in HM07, for two reasons. First, it allows us to use the published CDF-N image from A03, exactly the same image used for source detection. Second, it enables straightforward comparisons between our results and previous measurements of the soft X-ray $\log N$ – $\log S$, which usually are measured for 0.5–2 keV. One drawback of the 0.5–2 keV band is that it also includes significant diffuse signal at $E < 1$ keV from local and Galactic emission (HM06); however, this diffuse component can be accurately subtracted from the fluxes measured in the small *HST* source regions (see below), and so does not significantly affect the measured counts distribution. We assume that the fraction of the extragalactic CXB resolved by *HST* sources is the same in the 0.5–2 and 1–2 keV bands, since faint X-ray sources tend to have power law spectra with photon index $\Gamma \sim 1.4$, similar to the total extragalactic CXB (e.g., Rosati et al. 2002, see Fig. 13 of HM06).

A key element in this analysis is the background subtraction, since the background not associated with the *HST* sources is ~ 4 times larger than the source flux within the small source regions. Our background-subtraction procedure is different from that used in HM06 and HM07. Here the background consists of (1) local and Galactic diffuse sky emission, (2) flux from faint unresolved X-ray sources that do not have *HST* counterparts and whose positions we assume are random in the field, and (3) the instrumental back-

² For CDF-N images and exposure maps from A03, see <http://www.astro.psu.edu/users/niel/hdf/hdf-chandra.html>

³ Available at http://archive.stsci.edu/pub/hlsp/goods/catalog_r1/h_r1.1z_readme.html

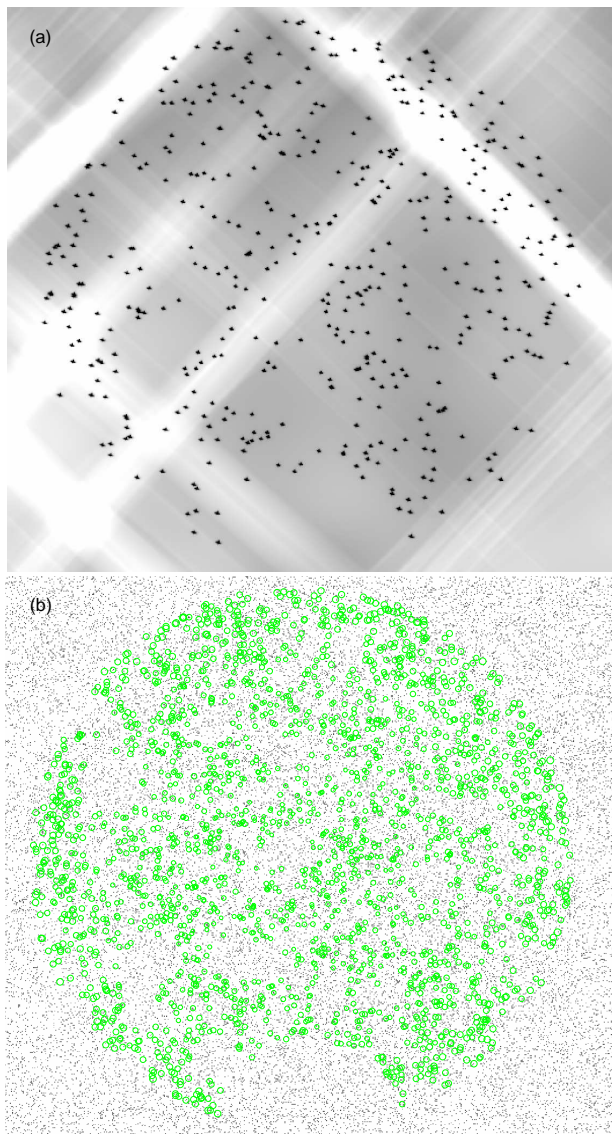


FIG. 2.— (a) Simulated photon probability map and (b) corresponding sky image, for a model in which all *HST* sources with X-ray counterparts have average fluxes of 2 counts per 2 Ms exposure. The extraction regions of radius r_{90} around all X-ray sources are shown in (b). The large empty regions within the area of radius $2.2'$ are the excluded regions around detected X-ray point and extended sources.

ground, with both quiescent and flaring components (see § 4 of HM06). The full 1.94 Ms image from A03 includes some flux from background flares, which can be eliminated using detailed light-curve analysis, as we did in HM06 and HM07. Here, in order to maximize the available exposure time we do not clean for flares. The flaring background is distributed nearly evenly across the X-ray image, so we can treat it as a component of the total diffuse background.

All the above components of the background are distributed relatively smoothly across the field of view, so we can accurately estimate the intensity and spatial distribution of the background by performing a wavelet decomposition (Vikhlinin et al. 1998) on the 0.5–2 keV image itself. The small-scale wavelet components include all detectable X-ray sources, while the largest scale ($40''$) component approximates the background. This component also includes signal from the X-ray-undetected *HST* objects, whose fluxes we

want to analyze. To remove this signal, we measure the number of 0.5–2 keV counts outside the *HST* and X-ray exclusion regions but inside the $2.2'$ circle, and then normalize the large-scale wavelet image to match the surface brightness in this area. We approximately account for the fact that 9.9% of the flux from the *HST* sources is scattered outside the r_{90} source regions. This normalization is given by

$$N_B = \frac{I_B - 0.099(I_{HST} - M_{HST}I_B/M_B)}{M_B}, \quad (2)$$

where I_B and M_B are the number of counts in the regions outside the *HST* and X-ray source regions and I_{HST} and M_{HST} are the total counts inside the *HST* regions, in the image (I) and unscaled wavelet background model (M), respectively. For the A03 0.5–2 keV image, $I_B = 14,691$, $M_B = 15,584$, $I_{HST} = 4806$, and $M_{HST} = 4175$ counts, resulting in $N_B = 0.937 \pm 0.08$ (1σ statistical error).

Subtracting this background leaves $I_{HST} - N_B M_{HST} = 894$ net counts associated with the *HST* sources. Using the average counts-to-flux conversion from A03 for sources within $2.2'$ of the aimpoint, this corresponds to a 0.5–2 keV surface brightness of $\sim 8 \times 10^{-13}$ ergs cm $^{-2}$ s $^{-1}$ deg $^{-2}$ over the 12.2 arcmin 2 area. Assuming a $\Gamma = 1.4$ power-law spectrum, this agrees well with the 1–2 keV brightness of 5.7×10^{-13} ergs cm $^{-2}$ s $^{-1}$ deg $^{-2}$ for the *HST* sources from HM07, derived from a completely different procedure.

To derive the distribution of source counts, we measure the counts in each of the 2184 *HST* source regions after subtraction of the “diffuse” background model and produce the distribution shown in Fig. 1. We include bins up to 15 source counts, which corresponds to the $\sim 70\%$ completeness limit for the source detection (B04). Although the histogram bins with ≥ 13 counts contain no sources, we include them because they help constrain some model flux distributions; the exact upper bound does not strongly affect our results.

Because many *HST* regions overlap, the total number of counts in the histogram is 1048, larger than the total of 894 counts mentioned above. We also determine the average exposure time for each *HST* region, which varies from ~ 1.2 Ms in the chip gaps to 1.94 Ms on axis, with a mean value of $\langle t_{\text{exp}} \rangle \simeq 1.8$ Ms; this is used below.

3.2. Comparison to $\log N - \log S$ models

To constrain the X-ray flux distribution of the undetected *HST* sources, we now compare the observed counts histogram to the predictions for various model $\log N - \log S$ curves. Poisson fluctuations cause the observed *counts* distribution to differ from the underlying *flux* distribution. In addition, we cannot simply evaluate predictions of the $\log N - \log S$ models analytically, because many source regions overlap and share the same photons, so we must account for the spatial distribution of the *HST* sources and the variation in the *Chandra* PSF. Therefore, we produce simulated X-ray images for each model $\log N - \log S$ distribution and then derive count histograms that we can directly compare to the CDF-N histogram. For each model $\log N - \log S$, we use the following procedure:

1. We produce a model flux distribution in units of 0.5–2 keV counts in 2 Ms (2 Ms rather than 1.94 or 1.8 Ms is used for simplicity). The fluxes S range from 0.05 to 30 counts per 2 Ms (which extends sufficiently above the source detection limit) in $n_{\text{flux}} = 600$ bins 0.05 counts wide. Our final results are not highly sensitive

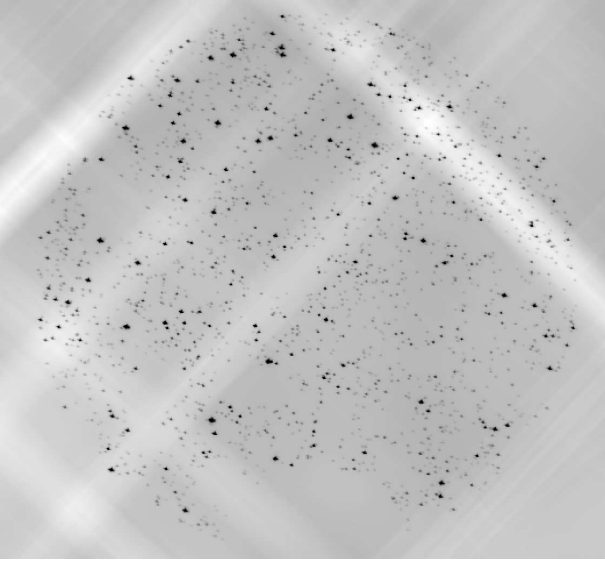


FIG. 3.— Probability map similar to Fig. 2(a), but for a power-law $\log N - \log S$ model with $\alpha = 1$.

to the flux bounds or bin size. We define $N_{\text{src}}(S)$ to be the number of sources in each bin of flux S in the 12.2 arcmin^2 area.

2. We normalize the flux distribution to produce, on average, the observed 894 total source photons in the *HST* regions. The 1σ statistical uncertainty in this value is ± 80 counts, mostly owing to fluctuations in the total counts before subtraction of background, but also includes uncertainty in the background normalization (Eqn. 2), which corresponds to ± 31 counts. The error on the total number of source counts corresponds directly to uncertainty in the normalization of the unresolved $\log N - \log S$ distribution. However, as we show in § 5.4, statistical fluctuations do not affect our constraints on the *shape* of the $\log N - \log S$ distribution, so for technical simplicity we ignore this uncertainty when constraining the $\log N - \log S$ slope.

In normalizing the model $\log N - \log S$ distribution, we account for the scattering of flux outside the r_{90} regions, as well as the probability that a source of a given flux would be detected in the CDF-N and not associated with the “unresolved” *HST* sources. For a given flux S , the average number of observed source counts inside the source regions is

$$S_{90}(S) = 0.9 \frac{\langle t_{\text{exp}} \rangle}{2 \text{ Ms}} S. \quad (3)$$

The average total number of counts, including background, in each r_{90} circle is

$$S_{\text{tot}}(S) = S_{90}(S) + \langle S_B \rangle, \quad (4)$$

where $\langle S_B \rangle = 2.03$ is the mean number of background counts per source region. For the purposes of normalizing the model $\log N - \log S$ only, we assume that the exposure time and number of background counts in all the *HST* source regions are equal to $\langle t_{\text{exp}} \rangle$ and $\langle S_B \rangle$, although they vary by up to 30%. As we show below, this gives a sufficiently accurate normalization to match the number of observed counts.

In the observed image, we have excluded detected X-ray sources using much larger regions of radii $> 4.5r_{90}$ to avoid PSF-scattered flux. To make the models consistent with this exclusion, we must remove sources from the simulated image that would be “detected” in the A03 catalog. For a given source flux, there is a probability (given by Poisson scatter and source detection completeness) that a source will be detected and thus removed from the image; we estimate this probability and include it in the normalization as follows.

For a given S and $\langle S_B \rangle$, the number of observed counts is determined by a Poisson distribution with mean S_{tot} . For j total counts, the measured source counts will be $S_j \equiv j - \langle S_B \rangle$. Here we define $f_c(S_j)$ to be the probability of detecting a source with S_j source counts within an r_{90} circle. We estimate f_c from the B04 completeness curve (which is for aperture-corrected total counts), by multiplying their x -axis by 0.9.

On average, the number of counts contributed by a source with flux S to the total source counts in the r_{90} regions around *undetected* sources is $S_{90}f_{\text{nondet}}$, where

$$f_{\text{nondet}}(S, \langle S_B \rangle) = \frac{\sum_{j=0}^{\infty} S_j P_P(j, S_{\text{tot}}) [1 - f_c(S_j)]}{\sum_{j=0}^{\infty} S_j P_P(j, S_{\text{tot}})}, \quad (5)$$

and where $P_P(j, S_{\text{tot}})$ is the Poisson probability of observing j counts for a mean of S_{tot} .

On average, the total number of background-subtracted source counts in all the r_{90} regions associated with X-ray-undetected *HST* sources is therefore

$$C_{\text{src}} = \sum_{i=1}^{n_{\text{flux}}} N_{\text{src}}(S_i) S_{90}(S_i) f_{\text{nondet}}(S_i, \langle S_B \rangle). \quad (6)$$

We normalize the model flux distribution $N_{\text{src}}(S)$ so that $C_{\text{src}} = 894$.

We stress that this normalization is not a free parameter that we fit to the observed histogram. Instead, we normalize the model $\log N - \log S$ *before* producing the simulated images, so that on average, they match the total number of source photons observed in the sky image. This normalization approach proves sufficient; the resulting simulated images (that properly include variations in the exposure, background, and PSF, as described in the following section) produce, on average, 886 counts from “undetected” *HST* sources, within 1% of the target value of $C_{\text{src}} = 894$. We stress again that uncertainty in this total of 894 counts does not affect our constraints on the $\log N - \log S$ shape, as we show in § 5.4.

3. If the normalized flux distribution contains more than $N_{\text{HST}} = 2184$ X-ray sources between 0.05 and 30 counts (that is, more than the number of X-ray-undetected *HST* sources), we truncate the distribution at the faint end and renormalize it so that

$$\sum_{i=1}^{n_{\text{flux}}} N_{\text{src}}(S_i) = N_{\text{HST}}, \quad (7)$$

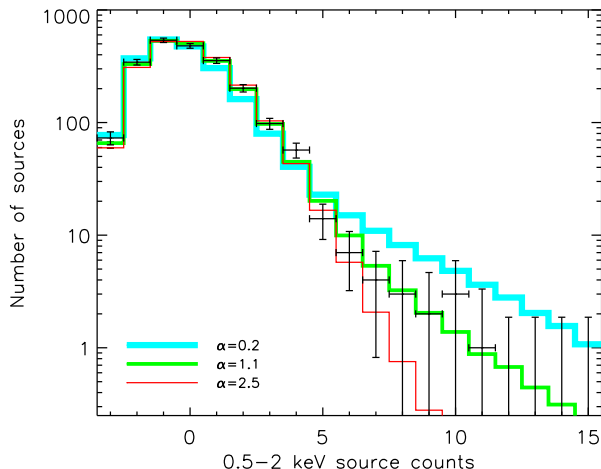


FIG. 4.— Same as Fig. 1, with models for power-law $\log N - \log S$ distributions.

while keeping $C_{\text{src}} = 894$ as per Eqn. 6. This effectively sets a minimum flux for the simulated X-ray sources. For the power-law models described below, this is required for slopes $\alpha \geq 1$. The cutoff is always at ≤ 0.3 counts per 2 Ms and does not significantly affect the final model fits (we might have used a more sophisticated $\log N - \log S$ distribution shape with a natural low-flux cutoff, but it is not warranted by the data). If the total number of sources turns out to be less than N_{HST} , we do not adjust the model flux distribution, since not all *HST* sources are necessarily X-ray sources.

4. We randomly assign fluxes to the 2184 *HST* positions from the distribution given by the normalized $N_{\text{src}}(S)$. For each source, we use a model of the *Chandra* PSF (from the *Chandra* CALDB) to create a 64×64 pixel X-ray probability map centered on the *HST* position, normalized to the model X-ray flux for that source and t_{exp} at the source position. The two-dimensional PSF model averages over the 20 constituent CDF-N observations that have different pointings (and thus off-axis angles) and exposure times.
5. We use the above model to create a simulated image of the sky. We produce Poisson realizations of the normalized background model (described in § 3.1) and of the probability maps for the sources, and add these realizations to create a simulated photon image.

In the process of creating this image, we eliminate “detectable” sources. Before adding each source to the image, we derive the total observed (post-Poisson scatter) source plus background counts I in the r_{90} circle. This corresponds to $I - S_B$ “measured” counts, where S_B is the value of the background model in the source region. Based on the probability $f_c(I - S_B)$ that this number of observed counts is detectable, we randomly assign the source as “detected” or “undetected”, and do not add detected sources to the simulated image.

We repeat steps 4 and 5 1000 times in order to average the random fluctuations in each simulated image. For each of these 1000 simulated sky images, we derive the number

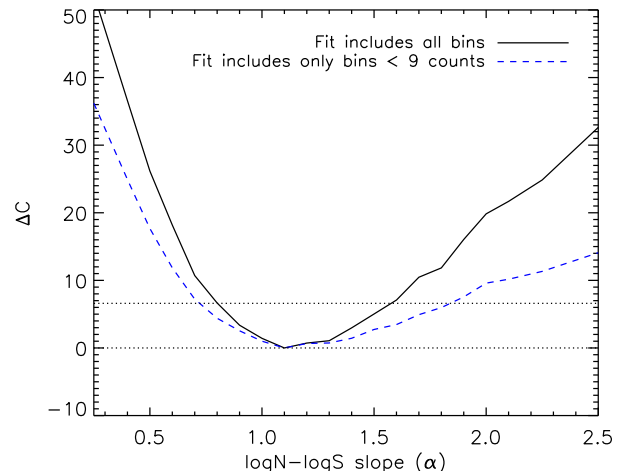


FIG. 5.— Variation in the C -statistic above the minimum (ΔC) vs. power-law slope α of the source flux distribution. The solid line shows the results using all histogram bins, while the dashed line shows results for only those bins with < 9 counts. The upper dotted line corresponds to the 99% confidence limit ($\Delta C = 6.6$).

of counts within r_{90} for each of the *HST* source regions, and produce a histogram of the background-subtracted counts, exactly as for the sky image. We average these 1000 histograms to produce a predicted counts distribution for this $\log N - \log S$ model and compare it to the observed one.

In comparing to the observed counts histogram, the χ^2 test is not appropriate because some of the bins have less than five sources, so the uncertainties are not Gaussian. Therefore, we calculate the best-fit model and parameter confidence intervals using the C -statistic (Cash 1979), which is valid for fits to bins with low numbers of counts and Poisson errors. The probability distribution of ΔC , which is the difference between C for the true value of the free parameter and its measured minimum in C , is similar to the χ^2 distribution for 1 degree of freedom, which we verify for our particular case using a simulation (described in § 5.4). Thus, a 99% confidence interval for one parameter corresponds to $\Delta C \simeq 6.6$. To calculate a rough goodness of fit (which is not determined by the C -statistic), we also estimate χ^2 , using errors (as shown in Fig. 1) given by $\sigma_n = (n + 0.75)^{1/2} + 1$, which is an approximation of Poisson uncertainties for n sources per bin (Gehrels 1986).

4. RESULTS

4.1. Delta-function flux distribution

As a simple but illuminating exercise, we begin with a “delta function” flux distribution, such that all the X-ray-undetected *HST* sources have either a single X-ray flux or zero flux [that is, $N_{\text{src}}(S_i) = 0$ for all but one S_i]. We produce model distributions for 0.5, 1, 1.5, 2, 3, and 4 photons per source per 2 Ms. A sample photon probability map and corresponding simulated image are shown in Fig. 2, and some of the resulting histograms are shown in Fig. 1. Because of Poisson fluctuations, even this simple flux distribution produces a quite broad distribution in the observed source counts.

Fig. 1 shows that if all sources below the detection threshold were relatively bright (with $S > 3$ photons in 2 Ms), this would produce too many *HST* sources with 4–8 observed counts

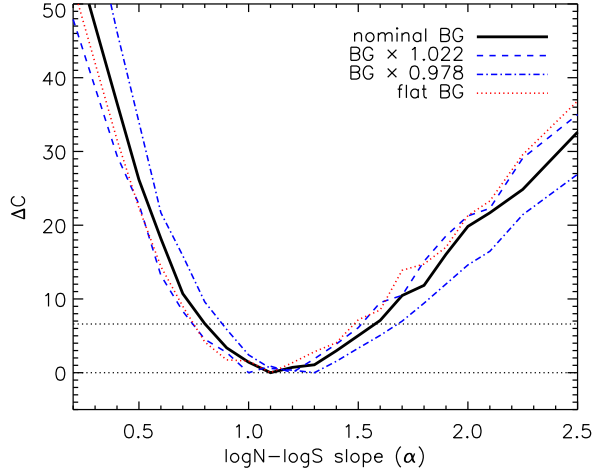


FIG. 6.— Same as Fig. 5, for different estimates of the diffuse background. The thick line shows ΔC vs. α for the background as calculated in § 3.1 (as in Fig. 5). The blue dashed lines show results for the same spatial distribution of the background, scaled by 1.022 and 0.978. The red dotted line shows results for a spatially uniform background, with a mean value as calculated in § 3.1. Varying the estimates of the background does not significantly change the constraints on α .

within their r_{90} source regions and too few with 1–2 counts. Conversely, a distribution with only very faint sources ($S \leq 1$ photon in 2 Ms) gives too few sources with 7–8 counts in the source regions. The data are fit well ($\chi^2 = 10$ for 18 degrees of freedom) if all the undetected sources have fluxes of 1.5–3 photons per 2 Ms.

4.2. Power-law flux distribution

The actual flux distribution for the *HST* sources is likely not a delta function. Here we consider the simple case of a power-law distribution $N(> S) \propto S^{-\alpha}$, with α between 0.2 (flatter than the faint-end slope of the total CDF $\log N - \log S$) and 2.5 (steeper than the observed $\log N - \log S$ for galaxies; see § 1). A sample photon probability map for a model with $\alpha = 1$ is shown in Fig. 3.

The resulting counts histograms for these models are shown in Fig. 4. The C-statistic is minimized at $\alpha = 1.1$, for which the data are fit well ($\chi^2 = 8$ for 18 degrees of freedom). Notably, the negative bins in Figs. 1 and 4 are well-described by all models, indicating that the statistical properties of the image are as expected and that we have properly accounted for background. The dependence of ΔC on α is shown by the solid line in Fig. 5. At 99% confidence ($\Delta C = 6.6$) we can rule out flux distributions with $\alpha < 0.8$ and $\alpha > 1.6$.

5. VERIFICATION

5.1. Background uncertainties

As described in § 3.1, the number of background photons in the *HST* source regions is ~ 4 times larger than the number of source photons, so our subtraction of the background is a key component of the analysis. Because we measure the spatial distribution and intensity of the background directly from the image itself, we expect our background model to be sufficiently accurate. Still, it is useful to check that the results do not depend strongly on our exact prescription for the background.

First, we note that the data histogram shown in Figs. 1 and 4, to which we perform the model fits, consists of counts *after*

subtraction of the background model. We use background-subtracted counts because they best represent the quantity of interest, which is the distribution of photons associated with the sources. Since the same background model is subtracted from both the data and the simulated images, we expect this procedure to have minimal effect on the parameter constraints. To verify this, we also calculate ΔC using the histogram of *total* observed counts with no background subtraction, and find that the confidence intervals are essentially identical (within $\approx 5\%$) for the two fits.

Next, we consider uncertainties in the (1) normalization and (2) spatial distribution of the background model. To address the impact of a different background normalization, we repeat the analysis for the $\log N - \log S$ models described in § 3.2, but vary the overall background level by $\pm 2.2\%$ (or 99% confidence intervals for the statistical error in the normalization given by Eqn. 2). This in turn changes the total number of photons associated with the *HST* sources (which is 894 for the nominal background) by $\pm 10\%$.

To address the effects of spatial variation, instead of using a wavelet map of the background that approximates the chip gaps and large-scale intensity variations, we repeat the analysis using a flat (spatially uniform) background, normalized using Eqn. 2, which gives a background of 0.101 counts pixel^{-1} . Each new background model produces a slightly different histogram of background-subtracted counts, in addition to new model distributions.

The values of ΔC versus α for these different background models are shown in Fig. 6. The variation in the background normalization changes the best-fit α by < 0.1 . Because the background normalization uncertainty is statistical in nature, we include this error in quadrature; it has only a small effect on our final constraints on α . These alternative backgrounds give similar goodness of fit ($6 < \chi^2 < 11$) to the nominal background.

5.2. PSF uncertainties

We have also considered uncertainties in our model of the *Chandra* PSF, since scattered flux between source regions may affect the count histograms. To test this dependence, we repeat the calculations, changing the width of the model PSF by $\pm 20\%$, or half the variation in r_{90} across our $2.2'$ region. We expect that the PSF model is significantly more accurate than $\pm 20\%$ (e.g., Allen et al. 2003), so this range is conservative. Although we change the PSF, we still use the r_{90} circles as defined in Eqn. 1 to derive the histogram of counts in the *HST* regions. Within this range of PSF widths, the flux scattered outside the r_{90} regions is between $\approx 7\%$ and 13% , which in turn affects our estimate of the background normalization N_B (as in Eqn. 2) by a small amount (≈ 0.0015), as well as our normalization of the model $\log N - \log S$ (as in Eqns. 3–6).

Properly accounting for these variations, we find that changing the PSF width by -20% has a negligible effect, while changing the PSF by $+20\%$ serves to increase the best-fit α by ≈ 0.2 . The wider PSF causes additional flux overlap between the individual sources, which produces more “undetected” sources with 8–15 counts and more strongly rules out models with low α . However, even for this conservative range of PSF widths, the uncertainty is still significantly smaller than our statistical upper bound on α . We conclude that PSF uncertainties have no significant effect on our constraints on the flux distribution.

There is a further slight uncertainty due to the fact that when we add the PSF models to the simulated images, the source

positions are rounded to the nearest pixel, creating a positional offset up to $0.35''$ between the model PSF in the image and the center of the source region. To verify that this does not affect our results, we repeated the analysis with the *HST* source regions shifted to account for this rounding offset; this produced negligible change in the constraints on α .

5.3. Source detection completeness

We further consider uncertainty in the model of the source detection completeness of the A03 catalog (given in B04), which may affect our modeling of the undetected *HST* sources with $\gtrsim 8$ source counts. For example, some of our input $\log N - \log S$ models are flatter, and have more overlap between bright sources than the model used by B04 to calculate the completeness limits. It is not immediately clear how this source overlap would impact the source detection completeness.

One simple test is to examine the variation in ΔC if we only include the bins at ≤ 8 counts, which are not strongly affected by the completeness estimates. This ΔC curve is shown by the dashed line in Fig. 5. Although these fits give slightly worse constraints on α , they are consistent with the results from the full histogram. To more rigorously examine the impact of the completeness, we repeat the full analysis using the simple case of a hard flux limit; all sources with > 8 source counts in the r_{90} circle are detected, and all others are undetected (corresponding roughly to the 9 count aperture-corrected limit for A03). To perform this comparison, we use only the histogram bins with ≤ 8 counts in the fits. This model gives nearly identical confidence limits (within 0.02 in α) to the more sophisticated completeness model described above. We conclude that uncertainty in the detection completeness given in B04 should not significantly affect the results.

5.4. Verification of the fitting procedure

Finally, we confirm the statistical validity of our constraints on α . In particular, we verify that (1) ΔC is distributed approximately like χ^2 for 1 degree of freedom in our particular case, and (2) our constraints are not affected by our normalization of the model $\log N - \log S$ distributions, which for computational simplicity we set to match the observed 894 source counts at the *HST* source positions (thus ignoring the $\pm 9\%$ 1σ statistical uncertainty in this value).

To this end, we perform a Monte Carlo simulation of the data and our fitting procedure, with two simplifications to allow for fast computations: we do not consider source overlap (so that counts observed at each source position are independent, and we do not need to create simulated images), and we do not account for the detection of bright sources, only considering sources with ≤ 10 observed source counts. We define a model power-law $\log N - \log S$ distribution with our best-fit value of $\alpha = 1.1$ and an average total flux of 1000 source photons observed at 2500 source positions. We also include a constant background flux of 2 photons per source.

We then create 1000 “observed” realizations of this flux distribution, in which fluxes are assigned randomly to the 2500 source positions. For each source, the observed counts are drawn from a Poisson distribution with a mean equal to the total source plus background flux. We then follow the fitting procedure outlined in § 3.2, and fit each realization of the data with model power-law $\log N - \log S$ distributions having slopes in the range $0.7 < \alpha < 1.6$. For each realization, we normalize the model $\log N - \log S$ to produce, on average, the number of total observed counts in that realization, rather than

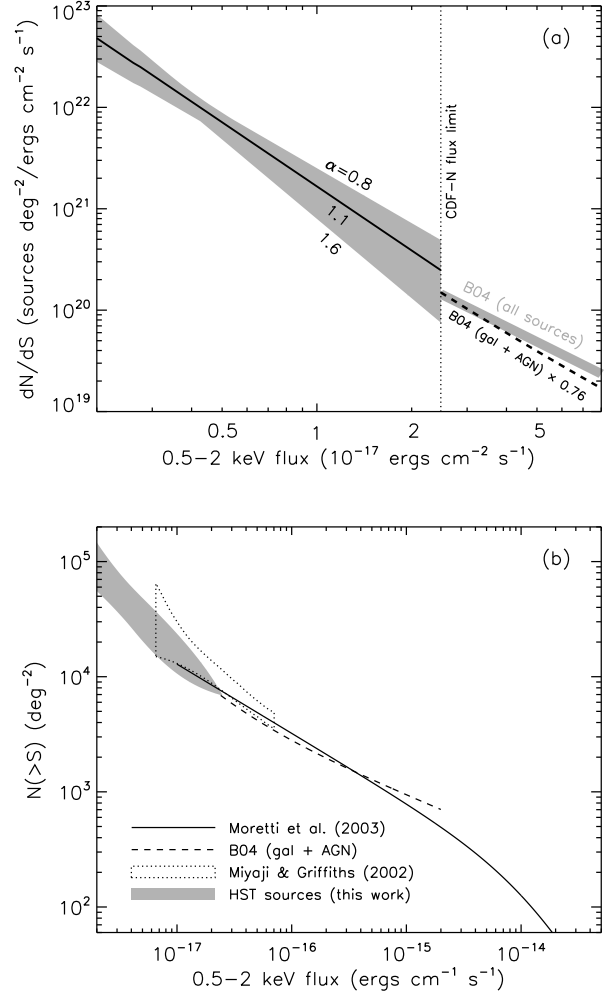


FIG. 7.— (a) The differential flux distribution (dN/dS) for unresolved *HST* sources, for the model power-law X-ray flux distributions allowed by the fits. The shaded area shows the 99% confidence intervals in power-law slope α and the normalization (see text for details). For comparison, the lines at right show the best-fit $\log N - \log S$ for all CDF-N sources (thick gray line) and AGNs plus galaxies (dashed line) from B04. For direct comparison with our model, the AGN plus galaxy curve is multiplied by 0.76 (see text). (b) The integral CDF $\log N - \log S$ distribution, showing best-fit curves from Moretti et al. (2003, solid line) and the AGN plus galaxy fit from B04 (dashed line). The gray area shows the 90% confidence intervals from the fluctuation analysis on the 1 Ms CDF-N exposure by Miyaji & Griffiths (2002). The hatched region shows the limits from the power-law fits to the unresolved *HST* sources, with $N(>S)$ set to equal the B04 galaxy plus AGN fit at $S_{0.5-2 \text{ keV}} = 2.4 \times 10^{-17} \text{ ergs cm}^{-2} \text{ s}^{-1}$. Note that our constraints provide only lower limits to the total X-ray flux distribution, since some X-ray sources might not be detected by *HST*.

the input average flux of 1000 source counts. In this way, we take into account statistical fluctuations in the total counts that we observe at the *HST* source positions.

For each realization, we calculate C versus α , and determine the best-fit α from the minimum in C . We find that in 99% of cases, the best-fit value of α lies $\Delta C < 6.6$ from the actual value of $\alpha = 1.1$. This confirms that (1) ΔC is distributed very similarly to χ^2 for 1 degree of freedom, and (2) that statistical fluctuations in the total observed counts do not affect our constraints on the slope α . These fluctuations do, however, introduce uncertainty in the $\log N - \log S$ normalization, which we include in our final results.

6. DISCUSSION

6.1. Constraints on the $\log N - \log S$ distribution

Our analysis shows that the distribution of photons in the CDF-N image associated with X-ray-undetected *HST* sources places significant constraints on their underlying flux distribution. Our final constraints on the slope are $\alpha = 1.1^{+0.5}_{-0.3}$. The corresponding normalization of the differential flux distribution is $dN/dS = (1.3 \pm 0.3) \times 10^{22}$ sources deg^{-2} ($\text{ergs cm}^{-2} \text{s}^{-1}$) $^{-1}$ at $S_{0.5-2 \text{ keV}} = 4 \times 10^{-18}$ $\text{ergs cm}^{-2} \text{s}^{-1}$ (all uncertainties are 99% confidence). In Fig. 7 (a), we show the dN/dS distributions allowed by the fits. The relatively small uncertainty at $S_{0.5-2 \text{ keV}} \sim 4 \times 10^{-18}$ $\text{ergs cm}^{-2} \text{s}^{-1}$ is a result of the fact that we restrict our $\log N - \log S$ models to be power-law in shape.

Our best-fit power-law model ($\alpha = 1.1$) connects well with that of the observed CDF-N $\log N - \log S$. In Fig. 7 (a) we compare it to the B04 fits for (1) the full CDF $\log N - \log S$, which has $\alpha \simeq 0.7$, and (2) the sum of the galaxies plus AGNs power laws fitted separately, which near the CDF-N flux limit can be approximated by a single power law with $\alpha \sim 1$. While these $\log N - \log S$ curves represent all X-ray sources, our fits constrain the flux distributions for *HST* sources only. Therefore, to account for the fact that only 16 out of the 21 detected X-ray sources in our 2.2' circle have *HST* counterparts, we show the B04 galaxy plus AGN curve multiplied by this fraction (0.76). At the CDF-N limit, the normalizations of both B04 curves are consistent with our allowed model distributions, but the slope of the AGN plus galaxy $\log N - \log S$ more closely matches our best-fit model for the fainter *HST* sources. This indicates that the X-ray-unresolved *HST* sources might represent the faint end of the resolved sub-population of normal and starburst galaxies, and that deeper *Chandra* observations might resolve significant numbers of these sources.

Fig. 7 (b) shows fits to the integrated $\log N - \log S$ in the CDFs. Shown are with the best-fit curve from Moretti et al. (2003), as well as the AGN plus galaxy fit from B04 (which only included sources fainter than $S_{0.5-2 \text{ keV}} = 2 \times 10^{-16}$ $\text{ergs cm}^{-2} \text{s}^{-1}$). We also show the constraints from our fits, by setting $N(> S)$ equal the B04 galaxy plus AGN curve at $S_{0.5-2 \text{ keV}} = 2.4 \times 10^{-17}$ $\text{ergs cm}^{-2} \text{s}^{-1}$ (this is necessary because we analyze only the *undetected* sources). The unresolved $\log N - \log S$ distributions allowed by our fits are consistent with the constraints obtained by the fluctuation analysis on the first 1 Ms of data by Miyaji & Griffiths (2002), and extend to lower fluxes.

6.2. Prospects for deeper *Chandra* exposures

How much of the remaining extragalactic CXB would be resolved by deeper *Chandra* exposures depends largely on the shape of the flux distribution for unresolved sources. For a shallow $\log N - \log S$ curve (i.e., low α), most of the unresolved CXB would come from relatively bright sources that could be detected with moderately deeper observations. For a steeper $\log N - \log S$, however, the bulk of the flux comes from much fainter sources.

As measured by HM07, 70% of the unresolved (or 16% of the total) 1–2 keV CXB is associated with *HST* sources. Fig. 8 shows the fraction of this flux that would be resolved as a function of survey depth, for the power-law $\log N - \log S$ models used in § 3. Here we consider the CXB to be “resolved” down to the flux of the faintest detected sources, ignoring incompleteness in the source detection (e.g., the A03 catalog is only $\sim 10\%$ complete at its nominal 9 count detection limit). The models with high and low α (Fig. 8, dotted

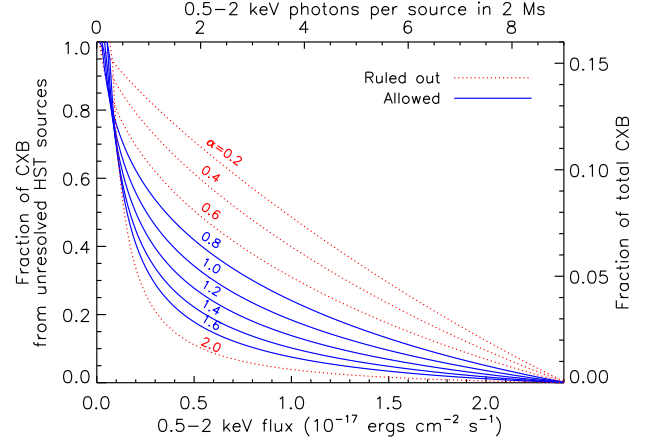


FIG. 8.— The fraction of the unresolved extragalactic 0.5–2 keV CXB from undetected *HST* sources that can be resolved as a function of limiting *Chandra* flux, for power-law model $\log N - \log S$ distributions. The current limit for 2 Ms is at the end of the x-axis. Models with $\alpha < 0.8$ and $\alpha > 1.6$ are ruled out by the model fits (see Figs. 5 and 6). The left y axis represents the flux associated with X-ray-undetected *HST* sources only (16% of the total soft CXB, HM07). The right y axis gives the corresponding fraction of the total CXB.

lines) are ruled out by our present analysis.

Let us consider further observations that are 5 times more sensitive than the current CDF-N, with a 0.5–2 keV flux limit of 5×10^{-18} $\text{ergs cm}^{-2} \text{s}^{-1}$. Source detection in such observations would likely become background-limited, so this sensitivity would require exposures more than 5 times the existing one. For these exposures, the range of α allowed by the fits ($0.8 < \alpha < 1.6$) corresponds to resolving between $\sim 20\%$ and 40% of 0.5–2 keV flux from the undetected *HST* sources. This would make up 13%–30% of the unresolved (or 3%–7% of the total) soft CXB. For the best-fit power law model with $\alpha = 1.1$, $\sim 30\%$ of the flux from the undetected *HST* sources would be resolved.

Of course, the present analysis does not constrain the fluxes from those undetected X-ray sources that do not have *HST* counterparts. Such sources can contribute up to an additional $\sim 30\%$ of the unresolved (or $\sim 6\%$ of the total) soft CXB. In the most optimistic scenario, all these sources would be detected in deep exposures, and the *HST* sources would have the flattest allowed $\log N - \log S$ slope. In this optimistic case, *Chandra* exposures 5 times more sensitive than the existing observations (i.e., > 10 Ms) would resolve up to $\sim 60\%$ of the remaining extragalactic soft CXB.

We thank A. Vikhlinin, C. Jones, R. Narayan, K. Lai, M. Weisskopf, and S. O’Dell for fruitful discussions and comments, and the referee for useful suggestions. R.C.H. was supported by a NASA GSRP Fellowship and a Harvard Merit Fellowship, and M.M. by NASA contract NAS8-39073 and *Chandra* grant G06-7126X.

REFERENCES

- Alexander, D. M., et al. 2003, *AJ*, 126, 539
Allen, C., Jerius, D., & Gaetz, T. 2003, in *CXC Calibration Workshop*
Bauer, F. E., et al. 2002, *AJ*, 123, 1163
Bauer, F. E., Alexander, D. M., Brandt, W. N., Schneider, D. P., Treister, E., Hornschemeier, A. E., & Garmire, G. P. 2004, *AJ*, 128, 2048
Brandt, W. N. & Hasinger, G. 2005, *ARA&A*, 43, 827
Brandt, W. N., et al. 2001, *AJ*, 122, 1
Cash, W. 1979, *ApJ*, 228, 939
Dickinson, M., Giavalisco, M., & The GOODS Team. 2003, in *The Mass of Galaxies at Low and High Redshift*, ed. R. Bender & A. Renzini (Berlin: Springer), 324
Gehrels, N. 1986, *ApJ*, 303, 336
Giavalisco, M., et al. 2004, *ApJ*, 600, L93
Hickox, R. C. & Markevitch, M. 2006, *ApJ*, 645, 95
—. 2007, *ApJ*, 661, L117
Miyaji, T. & Griffiths, R. E. 2002, *ApJ*, 564, L5
Moretti, A., Campana, S., Lazzati, D., & Tagliaferri, G. 2003, *ApJ*, 588, 696
Rosati, P., et al. 2002, *ApJ*, 566, 667
Vikhlinin, A., McNamara, B. R., Forman, W., Jones, C., Quintana, H., & Hornstrup, A. 1998, *ApJ*, 502, 558
Worsley, M. A., Fabian, A. C., Bauer, F. E., Alexander, D. M., Brandt, W. N., & Lehmer, B. D. 2006, *MNRAS*, 368, 1735